Auroral substorm timescales: IMF and seasonal variations

D. Chua,[1] G. Parks,[2] M. Brittnacher,[3] G. Germany,[4] and J. Spann[5]

Received 21 March 2003; revised 17 December 2003; accepted 24 December 2003; published 13 March 2004.

[1] The timescales and phases of auroral substorm activity are quantified in this study using the hemispheric power computed from Polar Ultraviolet Imager (UVI) observations. With this approach we are able to determine substorm phase self consistently from the UVI optical measurements without needing any ancillary metrics for auroral activity. This technique also allows us to combine a quantitative measurement of substorm timescales with the qualitative description of auroral morphology during each event. We show how the characteristics of substorms vary with IMF B_Z orientation and season for several hundred substorm events. Substorm intensity, as measured by the rate of energy deposition by electron precipitation, exhibits greater variation with IMF B_Z orientation than with season. The timescale of substorm expansion shows comparable variation with both IMF B_Z orientation and season. On the other hand, substorm recovery times vary more strongly with season than with IMF B_Z direction. The recovery time for substorm activity is well ordered by whether or not the nightside auroral region is sunlit: substorms occurring in the winter and equinox periods have similar recovery timescales which are both roughly a factor of two longer than that for summer when the auroral oval is sunlit. However, IMF B_Z orientation is shown to have a strong modulating effect on both substorm expansion and recovery timescales during the summer. The winter-summer asymmetries in the aurora described by previous studies are more completely explained by the seasonal variations of substorm recovery timescales characterized in this work. Our results support the hypothesis that the ionosphere plays an active role in governing the dynamics of the aurora. *INDEX TERMS:* 2704 Magnetospheric Physics: Auroral phenomena (2407); 2788 Magnetospheric Physics: Storms and substorms; 2431 Ionosphere: Ionosphere/magnetosphere interactions (2736); 2455 Ionosphere: Particle precipitation; *KEYWORDS:* substorms, timescales, conjugacy, season, aurora

Citation: Chua, D., G. Parks, M. Brittnacher, G. Germany, and J. Spann (2004), Auroral substorm timescales: IMF and seasonal variations, *J. Geophys. Res.*, *109*, A03207, doi:10.1029/2003JA009951.

1. Introduction

[2] The generic timescales of auroral substorms were described by *Akasofu* [1964] using a network of all-sky cameras in the auroral zone. In this seminal paper [*Akasofu*, 1964] established the characteristics of the average substorm with two distinct phases. In the expansion phase, a quiet auroral arc near magnetic midnight suddenly intensifies in brightness and rapidly moves toward the geomagnetic pole and outward in local time (longitude) over a period of tens of minutes at a rate of a few kilometers per second. The recovery phase begins once the substorm bulge dims and begins to retreat equatorward from its most poleward extent over timescales ranging from 30 minutes to about three hours. It should be stressed that the substorm description established by *Akasofu* [1964] distilled a large number of events into an average picture of the substorm sequence and the timescales associated with each phase. Individual auroral intensifications on the other hand exhibit a high degree of variability in their intensity as well as their expansion and recovery times. Quantifying the variability in these timescales is an essential task in further sorting out and understanding the physical processes underlying substorm phenomena.

[3] With its roots in the visual phenomenology of the aurora, the description of substorm timescales has remained largely qualitative since the work of *Akasofu* [1964] with some notable exceptions. Pi2 magnetic pulsations associated with impulsive magnetic field dipolarizations are commonly used to mark the onset of substorms [e.g., *Saito*, 1969; *Pytte et al.*, 1976; *Takahashi et al.*, 1995]. *Weimer* [1994] was one of the first to quantitatively examine the timescales of substorms, particularly those associated with substorm recovery. *Weimer* [1994] showed that the auroral electrojet (AE) index follows an exponential decay curve and attributed the characteristic substorm decay time to the

[1]Naval Research Laboratory, Washington, D. C., USA.
[2]Space Sciences Laboratory, University of California, Berkeley, California, USA.
[3]Department of Earth and Space Sciences, University of Washington, Seattle, Washington, USA.
[4]Center for Space Plasma, Aeronomic, and Astrophysics Research, University of Alabama in Huntsville, Huntsville, Alabama, USA.
[5]NASA Marshall Space Flight Center, Huntsville, Alabama, USA.

0148-0227/04/2003JA009951$09.00

fading of the westward electrojet. *Weimer* [1994] did not find a large variation in the values of the substorm decay (recovery) times which were on the order of 30 minutes. A slight trend of shorter decay times for larger substorms (with larger AE values) was found but no other variation was discussed.

[4] The results of *Weimer* [1994] are extended in this study in which we quantify auroral substorm timescales using the hemispheric power derived from Polar Ultraviolet Imager (UVI) [*Torr et al.*, 1995] measurements. We demonstrate that the exponential decay of the hemispheric power following an auroral substorm expansion provides a characteristic timescale, τ, for substorm recovery. This approach is advantageous because we can quantify substorm phase self consistently from the UVI optical measurements without needing any ancillary metrics for auroral activity such as the AE index. This technique also allows us to more precisely relate our quantitative measurement of substorm timescales with the qualitative description of auroral morphology during each event. We examine how substorm time scales vary with interplanetary magnetic field (IMF) orientation and season.

[5] We examine the IMF B_Z orientation as a relevant factor in controlling substorm timescales for the following reasons. During periods of southward IMF (negative IMF B_Z) magnetospheric convection is expected to be stronger in comparison to times when the IMF B_Z component is positive (northward). The effect of these two magnetospheric configurations on substorm timescales can thus be evaluated. The IMF B_Z component orientation is also important for two interpretations of activity associated with substorms: directly-driven phenomena and loading-unloading activity [*Rostoker et al.*, 1987; *Rostoker*, 1996]. In the former, a southward IMF condition leads to greater coupling between the solar wind and the magnetosphere presumably through enhanced dayside merging. Variations in the solar wind energy inputs are then directly manifested in the magnetosphere without inductive storage in the magnetotail. On the other hand, energy derived from the solar wind can also be inductively stored in the magnetotail field under southward IMF conditions (loading) and impulsively released into the auroral ionosphere and inner-magnetosphere during substorms (unloading). The unloading of magnetotail energy has been associated with northward turnings of the IMF which is often cited as a trigger for substorm expansion [*Caan et al.*, 1977; *Rostoker*, 1983; *Lyons et al.*, 1997].

[6] Our investigation into the seasonal variation of substorm timescales is motivated by a growing body of evidence establishing a seasonal asymmetry in the global characteristics of the aurora whereby discrete auroral forms are suppressed in a sunlit ionosphere. This has been shown using both spacecraft measurements of precipitating electron energy flux [*Berko and Hoffman*, 1974; *Newell et al.*, 1996] and auroral imaging techniques [*Petrinec et al.*, 2000; *Liou et al.*, 2001; *Shue et al.*, 2001; *Chua*, 2002]. A thorough review of seasonal variations in the aurora is given by *Newell et al.* [2001a] who left open the question of how the dynamics of substorms are affected by seasonal variations. Previous studies of seasonal variations in the aurora have focused on how the spatial structure and intensity of discrete aurora change with varying levels of solar insolation or ionospheric conductivity. We will focus on the seasonal dependencies of the temporal variations and timescales of auroral activity which have not been previously addressed in this context. One objective of this study is to further evaluate the hypothesis that ionospheric conductivity plays a major role in the large-scale dynamics of the aurora.

2. Substorm Phases Defined by Hemispheric Power

[7] One of the primary quantities derived from Polar UVI auroral images is the precipitating electron energy flux. The method used to infer the incident electron energy flux from Polar UVI images has been described in detail by *Germany et al.* [1994, 1998] and it will only be briefly summarized here. Polar UVI observes the Lyman-Birge-Hopfield (LBH) band of ultraviolet auroral emissions arising from electron impact excitation of N_2. In addition to the aurora, thermospheric airglow also contributes to the UVI images. These emissions are caused by photoelectrons produced by solar EUV radiation as well as resonantly scattered solar FUV photons. Quantitative analysis of the auroral emissions observed by UVI requires the subtraction of these airglow emissions. Following a procedure similar to that described by *Lummerzheim et al.* [1997], we assume that pixels corresponding to the same solar zenith angle (SZA) record similar airglow intensities. The image intensities are thus binned according to solar zenith angle excluding those pixels that fall within the auroral zone. The binned airglow flux versus solar zenith angle is then modeled using a least squares fit to a cosine squared function of the form

$$I_{dayglow} = I_0 \cos^2 (I_1 \Phi_{SZA}) \quad (1)$$

where Φ_{SZA} is the solar zenith angle. I_0 and I_1 are the two parameters returned by the least squares fitting. I_0 is the dayglow intensity at zero solar zenith angle and I_1 is a dimensionless factor that governs how fast the dayglow intensity falls off for increasing SZA. The modeled dayglow intensity versus SZA is then projected into a two-dimensional image to match the viewing geometry of solar zenith angles for a given UVI image. The modeled dayglow surface is then subtracted from the original image to yield the auroral intensities.

[8] UVI observations include the longer wavelength portion of the LBH emissions in the LBH-long (hereafter LBHl) filter which has a bandpass of 160–180 nm. At these wavelengths the attenuation of the LBH emissions by Schumann-Runge O_2 absorption is minimal. Therefore the intensity of the emissions observed in the LBHl filter is proportional to the amount of incident electron energy flux. Ignoring the dependence of this relationship on the average energy of the incident electron spectrum introduces a $\sim$10% systematic uncertainty in the energy flux computation but yields the advantage of a simple linear proportionality between the photon flux seen in the LBHl filter and the inferred electron energy flux.

[9] The computation of the hemispheric power from the UVI images is as follows. For each pixel (or spatial bin) in the LBHl images, the energy flux (ergs cm^{-2} s^{-1}) is inferred. We assume an emission altitude of 120 km and compute the projected surface area subtended by each pixel

at that height. Multiplying the energy flux by this area yields a measure of power. When integrated over the area of the auroral oval we obtain the hemispheric power (HP) which measures the rate at which energy is being deposited into the ionosphere by auroral electron precipitation. This is shown in equation (2) where $Q_{i,j}$ is the energy flux and $A_{i,j}$ is the area observed in each pixel (i, j). The computation of the hemispheric power from UVI images has also been described previously by *Lummerzheim et al.* [1997].

$$HP = \sum_{i=1}^{200} \sum_{j=1}^{228} Q_{i,j} A_{i,j} \quad (2)$$

[10] While the bulk of auroral power during substorms comes from the nightside auroral zone [*Newell et al.*, 2001b], we include all local times in the hemispheric power calculation. Limiting the hemispheric power integration to some range of local times invariably leads to an underestimation of the parameter in many cases due to the large variance in the local times in which the aurora expands during substorms. Tuning the limits of integration when computing the hemispheric power for each substorm event would be cumbersome for the large number of events that we examined for this study. Moreover, [*Newell et al.*, 2001b] found that the dayside auroral power showed very little variation during substorms. Inclusion of the dayside aurora in the total hemispheric power calculation only acts as an offset to the measurement. In general the entire auroral oval is observed in the UVI field of view for the events included in this study. However, in some cases a small portion of the dayside aurora is truncated out of the field of view during the viewing sequence. We simulated this circumstance using events with the full auroral oval in view and masking out 25% of the pixels on the dayside to evaluate the effect of this truncation on the hemispheric power calculation. We found that the effect was small with auroral power reductions less than or about 10% for the same two reasons given above: the nightside auroral power dominates over the dayside power and that the dayside auroral power does not vary significantly during substorms.

[11] The hemispheric power derived from the UVI images has a time resolution between 37 seconds and approximately six minutes depending on the mode in which UVI is operating. Since the hemispheric power is an integrated quantity, the Polar spacecraft's wobble [*Germany et al.*, 1998] has a negligible effect on this measurement under the assumption that flux is conserved regardless of how the measured photons are spatially distributed in an image. Distortion of the pixel areas due to the spacecraft wobble is only significant when the areas vary considerably from pixel to pixel as when observing near the limb. However, our observations are taken when viewing near nadir so we expect the area distortion to be a small effect.

[12] The hemispheric power derived from Polar UVI images has been shown to be a useful parameter for describing the rate of energy deposition by auroral electrons, particularly during large-scale auroral disturbances such as substorms. *Lummerzheim et al.* [1997] demonstrated that the temporal variability of the hemispheric power is better represented when derived from UVI images in comparison to extrapolating this parameter from in situ particle measurements along a single satellite track. *Newell et al.* [2001b] applied a superposed epoch analysis of Polar UVI derived hemispheric power to study the local time variations in auroral energy deposition during substorms. *Meng and Liou* [2002] have also argued that the Polar UVI derived hemispheric power can be used as an index for geospace activity and that it is well correlated with other such indices as the AE index.

[13] An example of how the hemispheric power varies over an auroral substorm is shown in Figure 1 for an event that occurred on 20 January 1998. The top panel shows the UVI-derived hemispheric power (in gigawatts) as a function of universal time. The dashed, vertical lines demarcate the substorm epochs to be defined using the hemispheric power as described below. Selected UVI images illustrate the global auroral morphology during each substorm epoch (phase). Each UVI image is shown in MLT-Apex MLAT coordinates [*Zandt et al.*, 1972; *Richmond*, 1995] and scaled in units of energy flux (ergs cm^{-2} s^{-1}). The B_Z (GSM) component of the interplanetary magnetic field (IMF) measured by the Magnetic Field Instrument (MFI) [*Lepping et al.*, 1995] aboard the Wind spacecraft is shown on the bottom panel of Figure 1. The Wind spacecraft was upstream in solar wind ($x_{GSM} = 232R_E$, $y_{GSM} = 18.3R_E$, $z_{GSM} = -13.0R_E$) and a propagation correction of 58 ± 21 minutes is applied to the IMF data. The method used to propagate the IMF is described in Appendix A.

[14] Qualitative determination of the substorm onset time can be made by identifying the UVI image frame in which one first observes an increase in luminosity prior to the expansion of the nightside auroral oval. In Figure 1 the onset of the substorm is identified in the 03:42:53 UT image as an enhancement of the precipitating electron energy flux between 2000–2300 MLT (Figure 1, Image B). *Liou et al.* [1999] and *Newell et al.* [2001b] have shown that substorm onset times can be determined from Polar UVI images with uncertainties on the order of three minutes. Using the hemispheric power we can define the onset (T_{onset}) of the auroral substorm more precisely as the time when this parameter increases above one standard deviation of the values in the preceding 30 minutes. Here, the uncertainty in identifying the substorm onset time is determined by the cadence at which LBHl images are obtained by UVI. For the observations shown in Figure 1, LBHl images with 37-second integration times are taken every three minutes and given that the image time labels correspond to the beginning of each (37-second) integration, the range of possible substorm onset times is 03:40:26–03:43:30 UT.

[15] We define the next substorm epoch as the period of time between substorm onset (T_{onset}) and when the hemispheric power reaches its peak ($T_{onset} - T_{HP_{max}}$). This epoch is equivalent to the canonical expansion phase of a substorm. In Figure 1 this is shown between 03:42:53–04:07:25 UT when the hemispheric power increases from about 15 GW to 63 GW. Both the precipitating electron energy flux and the observed surface area of the auroral oval increase during this interval (Figure 1, Images B–D). The slope of HP curve is generally positive during this time. The substorm epoch $T_{onset} - T_{HP_{max}}$ ends when the auroral oval has expanded to its greatest poleward and westward extent.

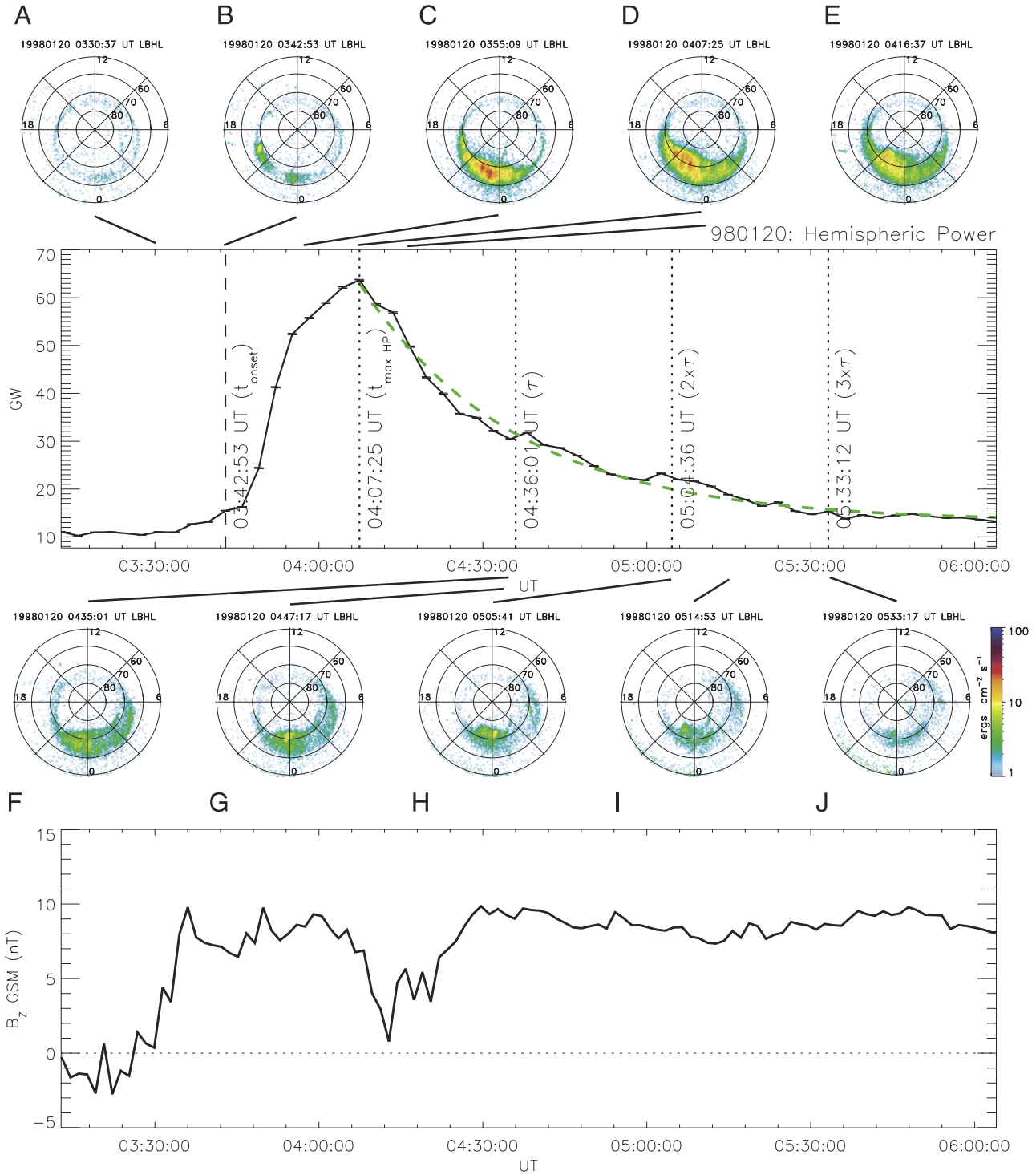

Figure 1. Hemispheric power for an isolated substorm on 20 January 1998 during northward IMF conditions. The dashed line beginning at 04:07:25 UT ($T_{HP_{max}}$) shows the least-squares fit of the HP to an exponential function given by equation (3). The vertical dotted lines denote the substorm epochs as described in the text. UVI images are shown at key times during the event.

This corresponds to the time when the precipitating electron energy flux is most intense (Figure 1, Image D) and the hemispheric power has risen to its maximum value following the onset of the substorm.

[16] The rate at which energy is deposited in the upper atmosphere by auroral electrons decreases exponentially after reaching its peak value. This decay of the hemispheric power is described by

$$HP(t) = HP_{max}e^{\frac{-t}{\tau}} + HP_o \quad (3)$$

Here HP_{max} is the maximum enhancement of the hemispheric power above its pre-onset value during a substorm.

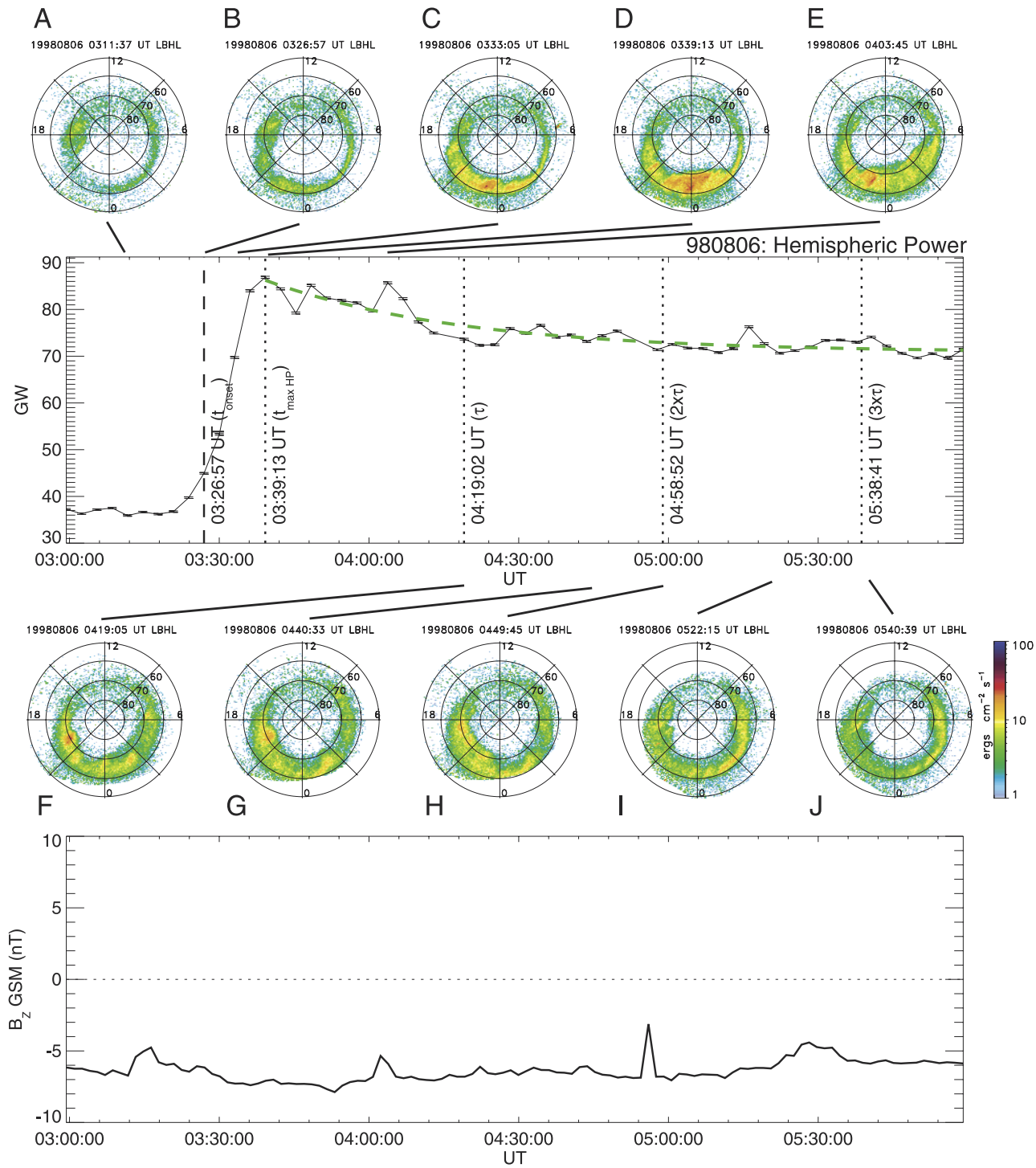

Figure 2. Same format as Figure 1 but for a substorm occurring during southward IMF. Note that the hemispheric power is sustained above its preonset level past three HP *e*-folding times.

HP_o is the asymptotic value of the hemispheric power during substorm recovery and represents the quiet time, baseline value of the energy deposition by auroral electrons. The *e*-folding time, τ, provides a fiducial time with which to define the next epoch of a substorm. This is the interval between the time of the maximum increase of the hemispheric power and the *e*-folding time ($T_{HP_{max}} - \tau$). In the example shown in Figure 1, the hemispheric power peaks at 04:07:25 UT. The *e*-folding time given by fitting the hemispheric power after $T_{HP_{max}}$ to equation (3) is 28.6 ± 0.9 minutes, shown at 04:36:01 UT. The epoch between $T_{HP_{max}}$ and τ is the beginning of substorm recovery. During this period, the hemispheric power decreases through the reduction of the precipitating electron energy flux since the area of the auroral oval does not change significantly between 04:16 UT and 04:36 UT (Figure 1, Images E–F).

[17] Subsequent substorm epochs are defined as multiples of the hemispheric power *e*-folding time: τ - 2τ and 2τ - 3τ. These are marked at 05:04:36 UT and 05:33:12 UT respectively in Figure 1. By 3τ the hemispheric power has recovered to just above its pre-onset value near 15 GW.

[18] The substorm event shown in Figure 1 is typical of substorms that occur when the B_Z component of the IMF is predominantly northward. The hemispheric power behaves in a slightly different manner during substorms for which the IMF B_Z is southward. An example of this is shown in Figure 2 which is presented in the same format as Figure 1. The IMF B_Z component remains at a steady southward value near -6.5 nT throughout the duration of this substorm (Figure 2, bottom panel). Following the onset and expansion of the auroral oval (Figure 2, Images B–E), the hemispheric power does not decay back to its pre-onset level as in the northward IMF case. By three *e*-folding times (3τ) the hemispheric power is still a factor of two higher than it was before substorm onset and is sustained primarily by aurora with precipitating energy fluxes above 10.0 ergs cm^{-2} s^{-1} along the dawn and dusk flanks of the auroral oval. The hemispheric power *e*-folding time for this southward IMF case is slightly longer at 40 minutes in comparison to the northward IMF event shown in Figure 1.

[19] Figure 2 also demonstrates that the hemispheric power sometimes exhibits aperiodic enhancements superposed upon the exponential decay. Some of these appear between 04:30–05:00 UT (Figure 2) and are due to small-scale intensifications within the auroral oval rather than from any ensuing global-scale activations of the aurora such as those seen during multiple onset substorms (Images F and G, Figure 2). Although these aperiodic hemispheric power enhancements increase the uncertainty in the determination of the hemispheric power *e*-folding times, we do not make any attempt to remove them prior to fitting the data to equation (3).

3. Statistical Analysis of Substorm Parameters

[20] Using the framework described above we have examined over 300 substorm events that occurred under a variety of solar wind conditions and in all seasons. These observations span solar cycle 23 between 1996 and 2001. However, we neglect any solar cycle effects on auroral substorm activity in this study. We wish to measure the intensity and time scales of auroral substorms as quantitatively as possible using the UVI-derived hemispheric power. Therefore we do not qualitatively distinguish between pseudobreakups [*Elvey*, 1957; *Akasofu*, 1964; *Sergeev et al.*, 1986; *Ohtani et al.*, 1993; *Nakamura et al.*, 1994; *Aikio et al.*, 1999] and substorms in the auroral intensifications chosen for this study. One key criterion for our event selection was to avoid magnetic storm periods when there can be global auroral intensifications with distinct characteristics from isolated substorms [*Lyons et al.*, 2000; *Chua et al.*, 2001]. These are often associated with the arrival of strong solar wind pressure pulses driven by coronal mass ejections (CMEs) that lead to magnetospheric compression and storm sudden commencement (SSC).

3.1. IMF Influence on Substorm Hemispheric Power

[21] The temporal behavior of the hemispheric power was shown in Figures 1 and 2 to depend on the IMF B_Z orientation. The hemispheric power decays back to pre-onset values for northward IMF substorms, while it is sustained above pre-onset values (past 3τ) for events in which the IMF is southward. To demonstrate this behavior in a more general sense, we perform a superposed epoch analysis of the hemispheric power values for substorms occurring during northward IMF versus those that occur when the IMF is southward (Figure 3). The criterion used to determine the IMF B_Z orientation is given in Appendix A. Universal time during each event is normalized to the substorm epoch fiducial times described above (T_{onset}, T_{HPmax}, τ, 2τ, and 3τ). The hemispheric power data are normalized to the maximum values for each event. The hemispheric power values are averaged within each substorm epoch and at each fiducial time for 86 events with northward IMF and 263 substorms with southward IMF. Figure 3 shows that the hemispheric power is maintained at about 13% above pre-onset values beyond three *e*-folding times of the HP parameter for substorms during southward IMF. On the other hand, the hemispheric power falls near

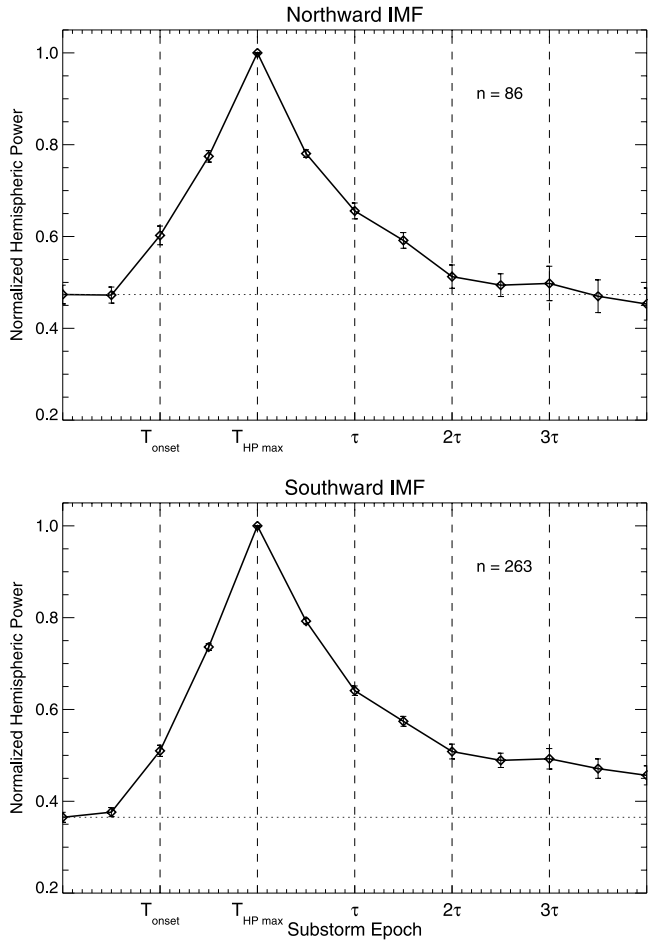

Figure 3. A superposed epoch analysis is performed on the hemispheric power for substorms that occur when the IMF is northward (top panel) versus southward (bottom panel). The hemispheric power values are normalized to the peak value for each event. Universal time is normalized to the substorm epochs defined in section 2. The error bars are the standard deviation of mean hemispheric power value for each epoch.

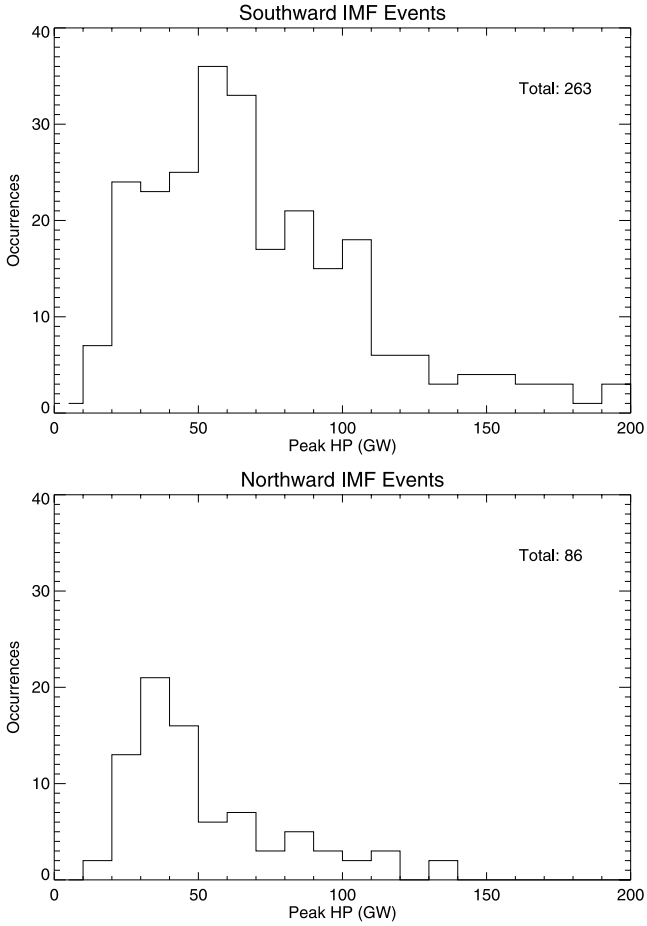

Figure 4. Histograms of the peak hemispheric power values for substorms sorted by IMF B_Z orientation.

the pre-onset values by two *e*-folding times for northward IMF events.

[22] To further investigate the effects of IMF B_Z orientation on substorm dynamics, we examine the statistical distributions of four parameters determined by the UVI-derived hemispheric power: (1) peak hemispheric power, (2) substorm expansion times, (3) hemispheric power *e*-folding times (τ), and (4) total hemispheric energy deposition. These parameters are sorted by northward versus southward IMF events using the criterion described in Appendix A.

[23] The distributions of peak hemispheric power values sorted by IMF orientation are shown in Figure 4 as histograms with 10 GW bins. The peak hemispheric power is an indication of the "size" or intensity of a substorm event. We find that the peak hemispheric power is about 30% on average greater for substorms that occur under southward IMF conditions versus those for which the IMF B_Z component is northward. The distribution of peak HP values for southward IMF substorms shown in Figure 4 has a mean value of 78.3 ± 52.9 GW whereas that for northward IMF substorms is 60.1 ± 50.3 GW (Table 1). In order to compare these distributions more rigorously, we compute a reduced chi-squared parameter given by equation (4).

$$\tilde{\chi}^2 = \frac{1}{d}\sum_{k=1}^{n}\frac{(D1_k - D2_k)^2}{D2_k} \qquad (4)$$

Table 1. Statistics for the Peak HP Sorted by IMF B_Z Orientation

Peak Hemispheric Power (GW)	Mean	Median	Standard Deviation
Southward IMF	78.3	65.8	52.9
Northward IMF	60.1	44.5	50.3

Here d is the number of degrees of freedom, taken as the number of bins, n, used to compute each distribution minus one. $D1$ specifies a distribution of some quantity and $D2$ is another distribution against which $D1$ is to be tested. $\tilde{\chi}^2$ values on the order of one or less ($\tilde{\chi}^2 \leq 1$) indicate that the two distributions are similar. If $\tilde{\chi}^2$ is much larger than one ($\tilde{\chi}^2 \gg 1$) then we expect $D1$ and $D2$ to be different. The degree of similarity between $D1$ and $D2$ is quantified by computing $P(\tilde{\chi}^2 \geq \tilde{\chi}^2_o)$, the probability of obtaining a $\tilde{\chi}^2$ as large as that computed from the observed distributions, $\tilde{\chi}^2_o$, given the number of degrees of freedom. These probabilities are calculated from the integral:

$$P\left(\tilde{\chi}^2 \geq \tilde{\chi}^2_o\right) = \frac{2}{2^{d/2}\Gamma(d/2)}\int_{\chi_o}^{\infty} x^{d-1}e^{-x^2/2}dx \qquad (5)$$

We use a standard criterion of specifying that two distributions disagree if $P(\tilde{\chi}^2 \geq \tilde{\chi}^2_o)$ is less than 5% [e.g., *Taylor*, 1982]. We find that the peak hemispheric power distributions sorted by IMF B_Z orientation are statistically

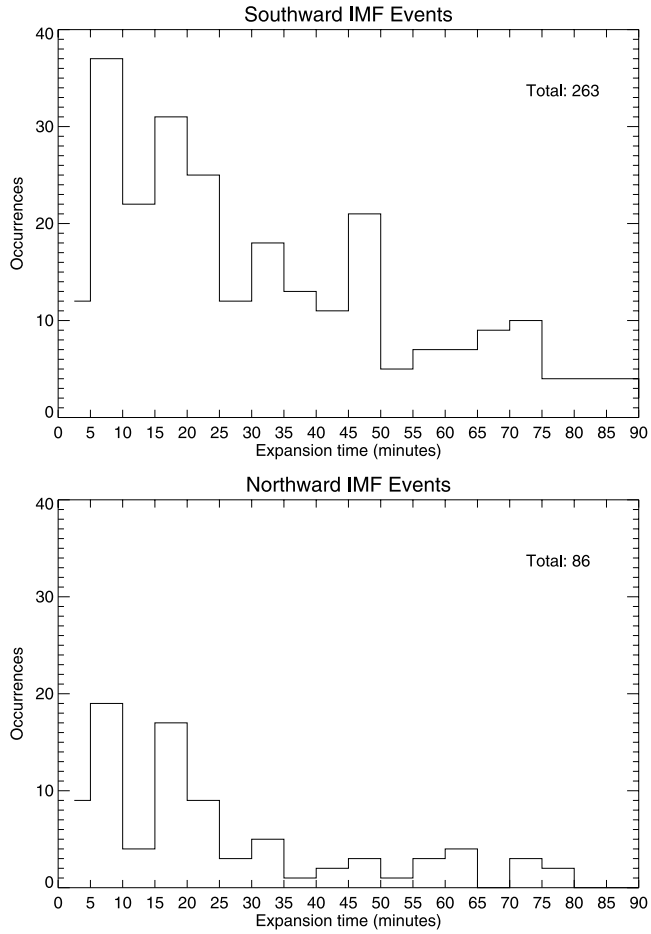

Figure 5. Histograms of substorm expansion times sorted by IMF B_Z orientation.

Table 2. Statistics for Substorm Expansion Times Sorted by IMF B_Z Orientation

$T_{onset} - T_{HP_{max}}$	Mean, min	Median, min	Standard Deviation, min
Southward IMF	36.1	32.6	27.6
Northward IMF	25.7	18.4	23.8

Table 3. Statistics for Substorm Recovery Times Sorted by IMF B_Z Orientation

HP *e*-folding times (τ)	Mean, min	Median, min	Standard Deviation, min
Southward IMF	32.8	30.0	19.1
Northward IMF	29.4	26.0	17.7

distinguishable and that the trend toward larger peak hemispheric power values for southward IMF substorms is significant ($\chi^2 = 6.4$, $P(\tilde{\chi}^2 \geq \tilde{\chi}_o^2) < 0.05\%$).

[24] We now examine the influence of IMF orientation on the times associated with substorm expansion ($T_{onset} - T_{HP_{max}}$) and recovery (τ). Figure 5 shows histograms of the substorm expansion times for events when the IMF B_Z is southward (top panel) or northward (bottom panel). The substorm expansion times in the northward IMF case have an average value of 25.7 minutes. We find that substorms for which the IMF is southward have a 40% longer expansion time, averaging 36.1 minutes (Table 2). This difference is significant ($\chi^2 = 4.9$, $P(\tilde{\chi}^2 \geq \tilde{\chi}_o^2) < 0.05\%$). Similarly we find that the hemispheric power *e*-folding times are about 12% longer for substorms under southward IMF than for those occurring under northward IMF (Figure 6). The hemispheric power *e*-folding times for the southward and northward IMF cases have mean values of 32.8 minutes and 29.4 minutes respectively (Table 3). The reduced chi-squared value when comparing these distributions of τ is 6.8 ($P(\tilde{\chi}^2 \geq \tilde{\chi}_o^2) < 0.05\%$) indicating that the longer hemispheric power *e*-folding times for southward IMF conditions is meaningful.

[25] Knowing the hemispheric power during a substorm and having quantitative measures of the times scales over which that power is supplied, we can readily compute the total energy input into the ionosphere (in one hemisphere) by auroral electron precipitation for each event. We compute the hemispheric energy deposition in Joules by integrating the hemispheric power from the substorm onset time to three HP *e*-folding times (3τ):

$$J_{HP} = \int_{t_{onset}}^{3\tau} HP \, dt \tag{6}$$

We sort the total energy deposition by IMF B_Z orientation and find that the energy input through auroral electron precipitation is greater by about 40% for substorms in which the IMF B_Z is southward (Figure 7). This result

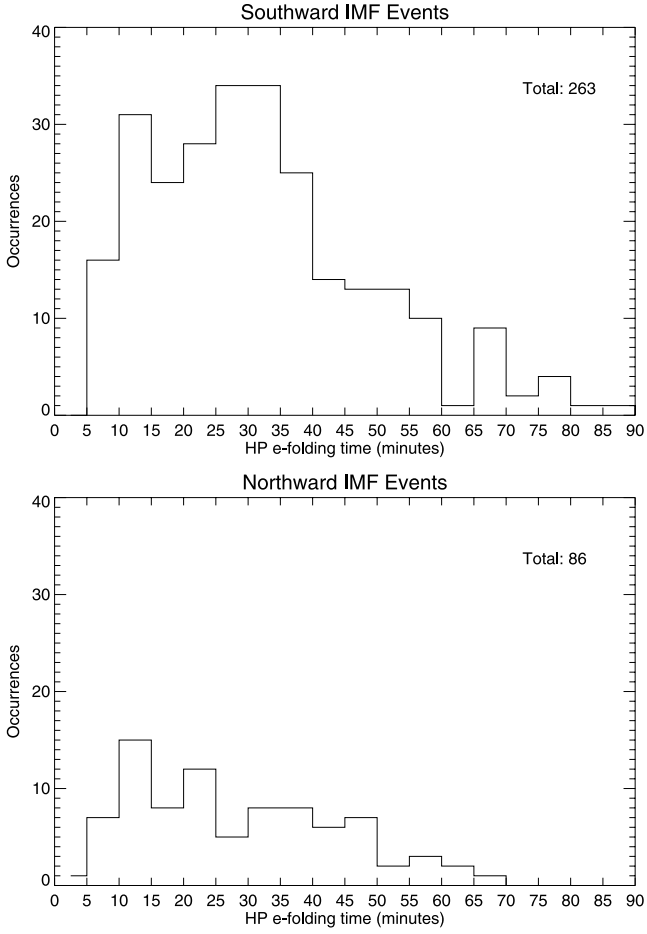

Figure 6. Histograms of the hemispheric power *e*-folding times sorted by IMF B_Z orientation.

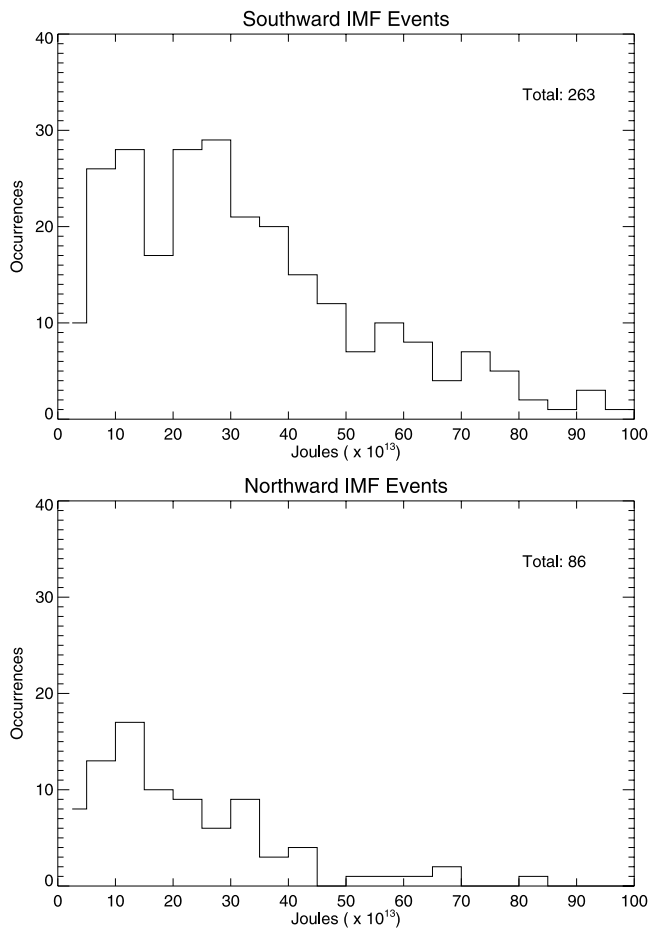

Figure 7. Distributions of total energy dissipated during substorm events sorted by IMF B_Z orientation.

Table 4. Statistics for Total Energy Dissipated Sorted by IMF B_Z Orientation

Total Energy Deposited	Mean ($\times 10^{13}$Joules)	Median ($\times 10^{13}$Joules)	Standard Deviation ($\times 10^{13}$Joules)
Southward IMF	36.2	29.1	31.5
Northward IMF	23.0	17.7	19.2

follows from the tendency for substorms during which the IMF B_Z is southward to sustain a higher level of hemispheric power during substorm recovery as demonstrated in Figure 2 and Figure 3. The mean, median, and standard deviation values for the total substorm hemispheric energy deposition are given in Table 4. A comparison of the total energy deposition distributions for northward versus southward IMF gives a χ^2 value of 6.0 and $P(\tilde{\chi}^2 \geq \tilde{\chi}^2_o)$ less than 0.05%.

3.2. Seasonal Variations of Auroral Substorm Characteristics

[26] Building on previous statistical studies of seasonal variability in the aurora, we investigate how substorm timescales and energy deposition vary with season. Following the convention used by *Petrinec et al.* [2000], the seasonal periods used in this study are centered on each solstice and equinox, and are defined conveniently by day of year (DOY). Winter is defined as DOY 309-34 (5 November–3 February), spring is then DOY 35-125 (4 February–5 May), summer follows as DOY 126-217 (6 May–5 August), and autumn is DOY 218-308 (6 August–4 November). The given calendar dates are for non-leap years and apply to the northern hemisphere where all of our observations are taken. In this study, the spring and autumn seasons are combined into one equinoctial category as the physical conditions in the ionosphere are similar during these periods.

[27] To examine how the magnitudes of the substorms vary with season, we plot histograms of the peak hemispheric power for the events in each seasonal category (Figures 8 and 9). On average, the peak hemispheric power values are shown to be highest during equinox. While the equinox and summer peak HP distributions are statistically similar ($\tilde{\chi}^2 = 0.95$ and $P(\tilde{\chi}^2 \geq \tilde{\chi}^2_o) = 52.5\%$), the equinoctial distribution exhibits a more pronounced tail at peak HP values above 110 GW. The winter distribution of peak HP is not consistent with either the equinoctial data ($\tilde{\chi}^2 = 1.80$, $P(\tilde{\chi}^2 \geq \tilde{\chi}^2_o) = 1.5\%$) or the summer peak HP distribution ($\tilde{\chi}^2 = 2.05$ and $P(\tilde{\chi}^2 \geq \tilde{\chi}^2_o) = 0.4\%$). However, the mean values of the peak hemispheric power during summer and winter differ by less than 0.6% with comparable standard deviations (Table 5). We do not find large differences in the seasonal distributions of peak hemispheric power. The peak hemispheric power distributions for each season are further sorted by IMF B_Z orientation. For each peak hemispheric power histogram shown in Figure 8 southward (northward) IMF events are shown in light (dark) gray. The same trends are observed here as when only sorting by IMF B_Z orientation. In each seasonal category, peak hemispheric power was higher by 20–40% for substorms in which the IMF was southward versus northward.

[28] The timescale of substorm expansion is found to be shortest during the summer. The average substorm expansion time during summer is 34% shorter than that for equinox and 25% shorter than the mean substorm expansion time in winter (Table 6). The reduced chi-squared test shows that the winter and equinox expansion time distributions are similar ($\tilde{\chi}^2 = 0.75$ and $P(\tilde{\chi}^2 \geq \tilde{\chi}^2_o) = 80.2\%$) as are the equinox and summer distributions ($\tilde{\chi}^2 = 1.38$ and $P(\tilde{\chi}^2 \geq \tilde{\chi}^2_o) = 10.2\%$). The chi-squared test distinguishes the winter and summer substorm expansion time distributions ($\tilde{\chi}^2 = 1.54$ and $P(\tilde{\chi}^2 \geq \tilde{\chi}^2_o) = 4.4\%$). For the winter and equinoctial periods, substorms during southward IMF have expansion times about 20–25% longer than those during northward IMF as we previously observed (Figure 5). However, for the summer time distribution, substorms occurring during southward IMF have an average expansion time that is almost a factor of two greater than those during northward IMF: 29.8 ± 23.3 minutes for southward IMF substorms versus 16.4 ± 14.8 minutes for northward IMF events).

[29] The largest difference in the seasonal characteristics of substorms comes when we examine the hemispheric power *e*-folding times (Figure 10). The distribution of substorm decay times for substorms in sunlit conditions is peaked between 10–15 minutes, with a mean value of 25.6 minutes (Table 7). The mean values of τ for the winter and equinoctial substorms are similar at about 35 minutes. The winter and equinox HP *e*-folding time distributions peak at a τ value which is about a factor of two greater than that seen during the summer. The median τ values for winter and equinox are comparable and each almost twice as long as the median HP *e*-folding time for summer. The reduced chi-squared value when comparing the winter-time τ values to those during summer is 10.0. Likewise, $\tilde{\chi}^2 = 5.6$ when comparing the hemispheric power *e*-folding times during equinox and summer. These reduced chi-squared values correspond to $P(\tilde{\chi}^2 \geq \tilde{\chi}^2_o)$ values less than 0.05%. In contrast we find that the winter-time and equinox distributions of τ are similar with $\tilde{\chi}^2 = 1.33$ and $P(\tilde{\chi}^2 \geq \tilde{\chi}^2_o) = 15.7\%$. The timescale for the persistence of substorm activity is a factor of two longer when the nightside auroral zone is in darkness (winter and equinox) than when it is sunlit. When subdividing the hemispheric power *e*-folding time distributions for each seasonal category by IMF B_Z direction, we find only minor variations for the winter and equinoctial events. During each of these seasons the average hemispheric power *e*-folding times varied by less than 10% for substorms with southward versus northward IMF. The effect of varying IMF B_Z orientation on the hemispheric power *e*-folding times is more pronounced during the summer as we also observed for the substorm expansion times. The average hemispheric power *e*-folding time for summer time substorms with southward IMF is 28.1 ± 24.1 minutes versus 19.3 ± 10.4 minutes for northward IMF events. Summer time substorms during southward IMF have hemispheric power *e*-folding times that are on average, 46% longer than those during northward IMF.

[30] The total energy deposited by auroral electrons during substorms is found to be greatest for equinoctial substorms, lower for winter substorms, and lowest for

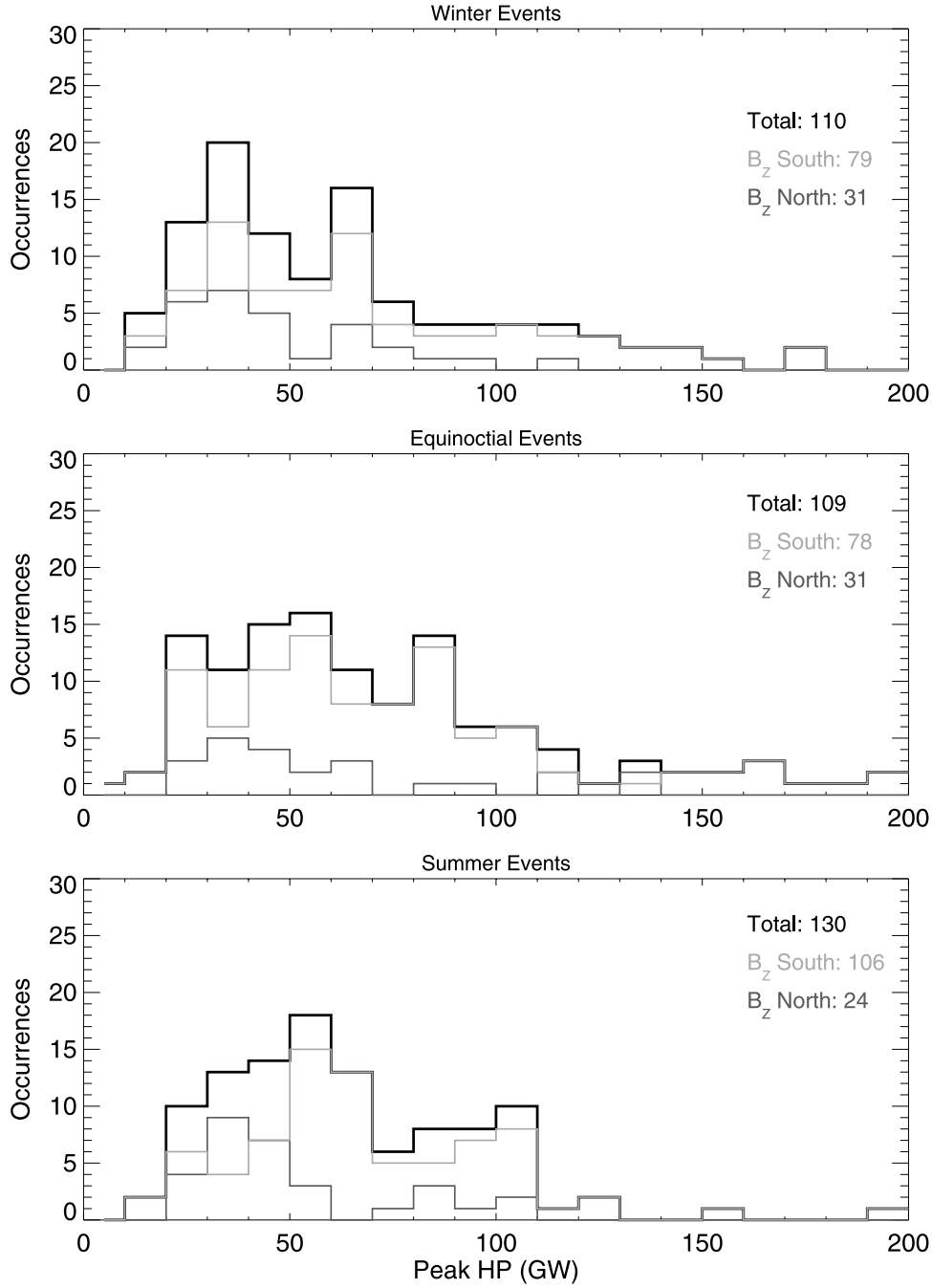

Figure 8. The peak enhancement of the hemispheric power above its pre-onset values for substorms occurring in winter (top panel), equinox (middle panel), and summer (bottom panel) conditions are shown in these histograms. For each season, southward (northward) IMF events are shown in light (dark) gray. One sees that the distributions of peak HP enhancement are not significantly different for events occurring in different seasons.

substorms occurring in sunlit conditions (Figure 11). This is consistent with the observation that substorms during all seasonal conditions have comparable energy deposition rates (Figure 8) but different recovery timescales (Figure 10): the total energy deposited during a substorm in the equinoctial and winter periods is higher than during the summer because the enhanced hemispheric power associated with auroral electron precipitation is sustained for longer periods of time. The winter-time and summer total energy deposition distributions are comparable ($\tilde{\chi}^2$ = 1.5 and $P(\tilde{\chi}^2 \geq \tilde{\chi}^2_o)$ = 7.7%) and both differ from the equinoctial distribution of total energy deposition. The average total energy deposition during the equinox periods is 41% greater than that in summer and 26% larger than that during winter (Table 8). When testing the equinox distribution of total energy deposition with each of the winter-time and summer ones, the reduced chi-squared values are greater than 2.25, giving $P(\tilde{\chi}^2 \geq \tilde{\chi}^2_o)$ less than 0.05%. Sorting each seasonal

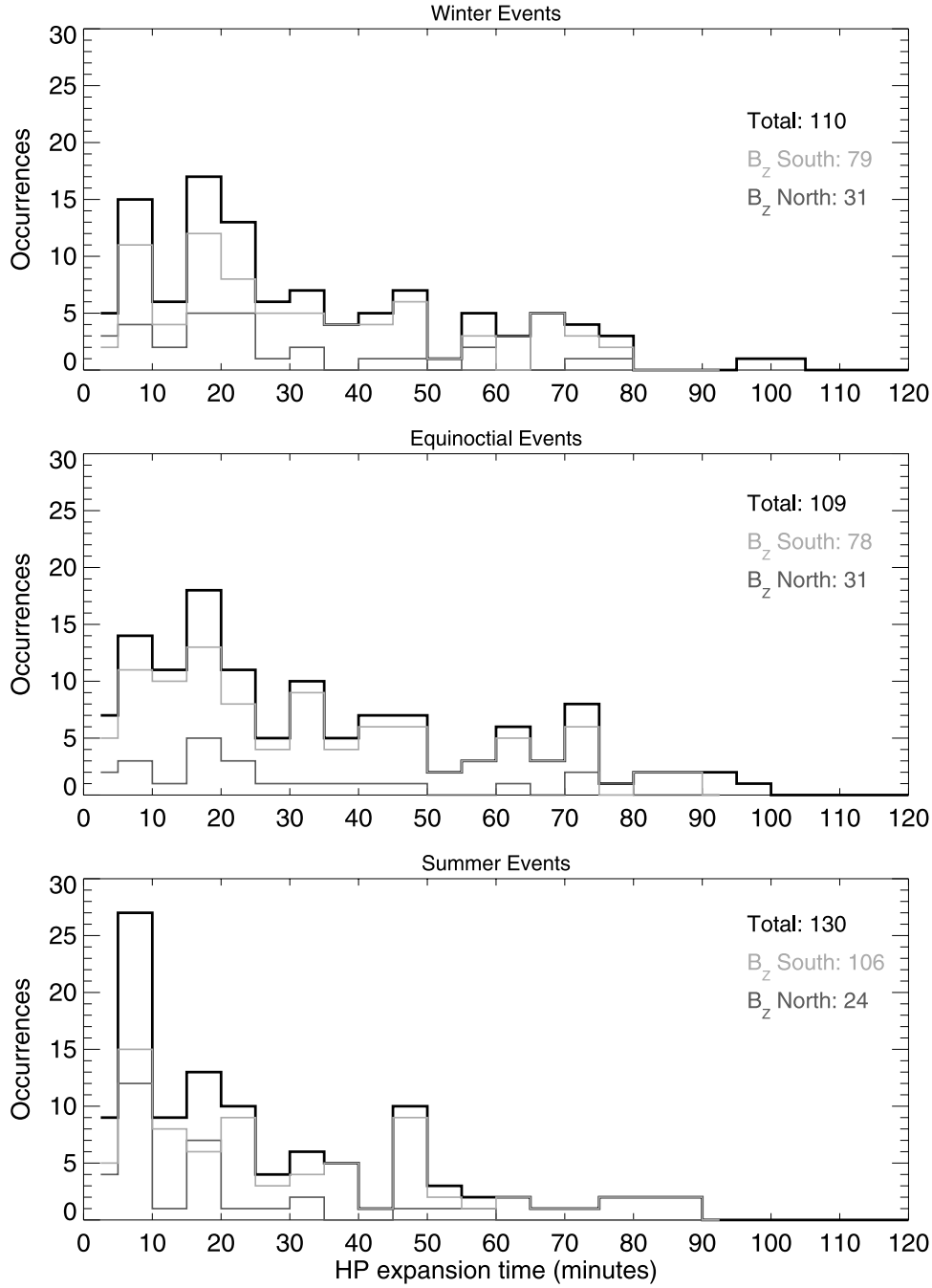

Figure 9. Seasonal distributions of substorm expansion times. The histogram in the top panel shows the distribution of substorm expansion times for events occurring in a dark (winter) ionosphere. The middle and bottom panel shows the expansion times for events occurring in equinox and summer (sunlit) conditions, respectively.

distribution of total energy deposition does not reveal any new behavior. Substorms that occur during periods of southward IMF consistently resulted in more energy deposition than those events during northward IMF for all seasons.

4. Discussion and Conclusions

[31] We have devised a new method for defining substorm phases based on the temporal behavior of the hemispheric power associated with electron precipitation. The derivation of hemispheric power from UVI images allows us to quantitatively measure four substorm parameters: (1) the peak hemispheric power value as an indicator of substorm intensity, (2) substorm expansion time, (3) the hemispheric power characteristic decay time (τ), and (4) the total hemispheric energy deposition by auroral electron precipitation during each substorm. These parameters were computed for over 300 substorms which were sorted by IMF B_Z orientation (southward or northward) and season (summer, winter, and equinox).

Table 5. Statistics for Peak HP Sorted by Season

Peak Hemispheric Power	Mean, GW	Median, GW	Standard Deviation, GW
Winter	68.7	57.5	49.5
Equinox	82.8	66.4	61.1
Summer	68.3	59.4	43.6

[32] We found that varying IMF B_Z orientation has the strongest effect on substorm expansion timescales and the total hemispheric energy deposition (J_{tot}). Substorm expansion times were found to be 40% longer for events under southward IMF conditions in comparison to northward IMF. The influence of southward versus northward IMF orientation for peak substorm power (HP_{max}) is distinguishable but the effect is not very large. On average we find that the peak hemispheric power was about 30% larger for substorms occurring during southward IMF B_Z than for events when the IMF was predominantly northward. The timescale of substorm recovery, as measured by the τ parameter, did not vary significantly when sorting by IMF B_Z orientation alone. Collectively, the average hemispheric power *e*-folding time was only 12% longer for substorms when the IMF was southward versus when it was northward.

[33] The timescales of substorms occurring during the summer are more sensitive to varying IMF B_Z orientation than during either winter or equinox. Substorm expansion timescales during summer periods are almost twice as long during southward IMF conditions than during northward IMF. Similarly, characteristic substorm recovery times are about 50% longer during southward IMF than when the IMF B_Z component is northward. In contrast, the variation of the substorm timescales and energy deposition parameters with IMF B_Z orientation during winter and equinox is small and comparable to the differences observed when sorting by IMF alone. The enhanced sensitivity of substorm timescales to IMF B_Z orientation during summer may be a manifestation of stronger coupling between the solar wind, magnetosphere, and ionosphere under sunlit conditions when conducting paths for the closure of currents flowing into and out of the ionosphere are readily available.

[34] The results of this study should be taken with two caveats. Our sampling of events is largely biased toward substorms for which the IMF B_Z component is southward (263 events) versus those in which it is northward (86 events). Secondly, our observations are limited to the northern hemisphere. Simultaneous, auroral observations in both northern and southern hemispheres are key to validating any generalizations about seasonal behavior of the aurora.

[35] The seasonal variations in substorm timescales described in this study have strong implications for auroral conjugacy. Our results imply that auroral intensifications develop differently in the northern and southern hemispheres during a substorm under solstitial conditions. During the same substorm, we expect the auroral breakup in the dark (winter) hemisphere to be more intense and longer lived than that observed in the sunlit (summer) hemisphere. This hemispheric asymmetry in the aurora also implies that more energy is deposited by electron precipitation in the winter hemisphere than in the summer one during a substorm. This behavior is consistent with the findings of *Papitashvili et al.* [2002] who used near-conjugate magnetometer measurements in Greenland and Antarctica to show that substorm expansions extend to higher latitudes in the dark (winter) hemisphere. A limited number of case studies using optical measurements have also reported these hemispheric asymmetries in substorm expansion [*Vorobjev et al.*, 2001; *Fillingim et al.*, 2003].

[36] Some insight into the degree to which magnetospheric processes influence the intensity and timescales of substorms comes from recent observations of magnetotail dynamics during auroral intensifications. A long-standing debate among researchers is how large and how long in duration an auroral disturbance must be for it to be considered a substorm. Short-lived auroral intensifications that do not expand are generally distinguished from s ubstorms as pseudobreakups. This problem has been recently revisited by *Fillingim et al.* [2001], *Fillingim* [2002], and *Parks et al.* [2002] who studied ion and electron distribution function measurements and magnetic field observations in the magnetotail from the Wind spacecraft when its ionospheric footprint was in the vicinity of auroral disturbances seen by Polar UVI. With these coordinated measurements it was found that plasma sheet dynamics during pseudobreakup-like activity and substorms are indistinguishable. The similarity of plasma sheet behavior during pseudobreakups and substorms suggests that what governs whether an auroral disturbance is short-lived or fully develops into an Akasofu-like substorm is largely determined elsewhere, perhaps in the auroral acceleration region just above the ionosphere or in the ionosphere itself.

[37] This conjuncture is consistent with our finding that substorm time scales are a strong function of season. The hemispheric power *e*-folding time is a factor of two shorter on average for substorms occurring when the nightside auroral zone is sunlit (summer) in comparison to when it is in darkness during the winter and equinox periods. Substorm expansion times are longest during equinoctial conditions, about 30% shorter during winter periods, and shortest during the summer (by almost a factor of two relative to equinox). The peak hemispheric power did not vary significantly as a function of season. Substorms that occur in the summer have similar peak intensities as those that occur under winter or equinox conditions. The last finding is significant because it suggests that our seasonal comparison of substorm timescales was not biased by any variations of the intensity of individual substorm events with season.

[38] The pattern of seasonal variation in substorm timescales is most consistent with the hypothesis that the state of the ionosphere, measured in terms of ionospheric conductivity or density, plays an active role in governing the dynamics of the aurora. The distributions of substorm expansion times and recovery times are similar for winter-

Table 6. Statistics for Substorm Expansion Times Sorted by Season

$T_{onset} - T_{HP_{max}}$	Mean, min	Median, min	Standard Deviation, min
Winter	34.3	24.6	29.0
Equinox	39.3	27.6	37.1
Summer	26.0	18.4	22.0

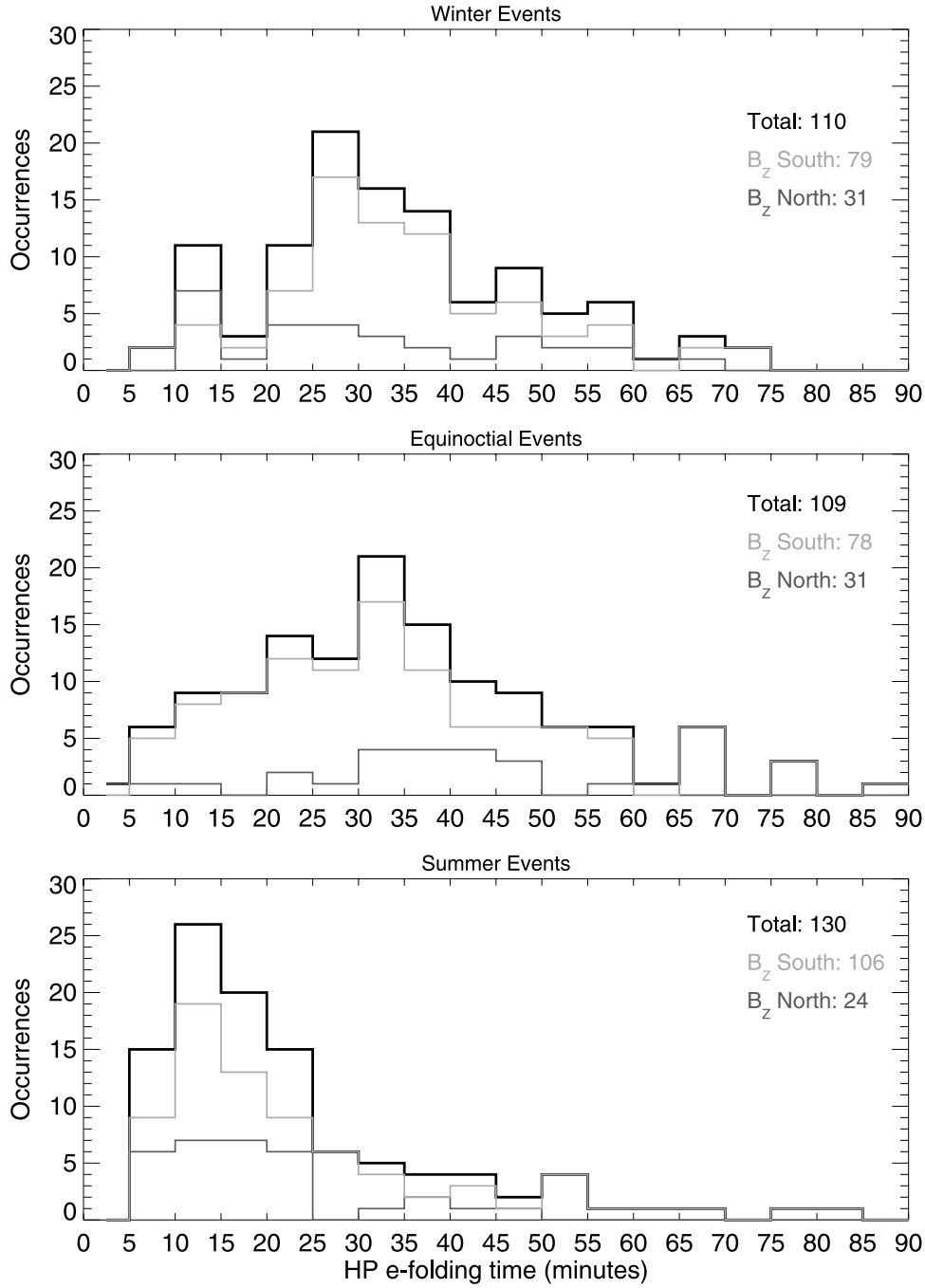

Figure 10. Seasonal distributions of substorm recovery *e*-folding times. The histogram in the top and middle panels show the distributions of *e*-folding times for events occurring in a dark (winter) and equinoctial ionosphere, respectively. The bottom panel shows a histogram of τ values for events occurring during summer.

time and equinoctial events when the nightside auroral zone is in darkness. When the nightside auroral zone becomes sunlit during summer periods the observed timescales of substorm activity shorten by about a factor of two. The dipole tilt angle of the earth's magnetic field does not appear to be an important factor in explaining the seasonal variability in our observed substorm timescales. The dipole tilt effect favors the equinoxes [*McIntosh*, 1959] while our observations show similar substorm characteristics during winter and equinoctial periods.

[39] The seasonal invariance of substorm peak hemispheric power and the shorter substorm timescales of substorms under sunlit conditions suggests a more complete picture than that found when one averages auroral characteristics over an entire season as earlier statistical studies of the seasonal dependence of auroral precipitation did. Although we have not described the relative contributions of discrete and diffuse precipitation in this study, we conjecture that the suppression of discrete aurora under enhanced ionospheric conductivity (sunlit conditions) is better explained by the

Table 7. Statistics for Substorm Recovery Times Sorted by Season

HP *e*-folding times (τ)	Mean, min	Median, min	Standard Deviation, min
Winter	34.1	31.9	14.9
Equinox	35.5	34.1	18.0
Summer	25.6	18.5	21.5

scenario of discrete auroral structures having shorter lifetimes in the sunlit hemisphere. To answer the question posed by *Newell et al.* [2001a], substorms do indeed occur under sunlit conditions in the auroral zone but with shorter timescales. The winter to summer ratio in seasonally averaged precipitating electron energy flux was found to be between 1.5 [*Liou et al.*, 2001] and 3.0 [*Newell et al.*, 1996, 2001a]. The factor of two difference in substorm recovery timescales between substorms occurring in darkness (winter and equinox) and those occurring under sunlit conditions (summer) found in this study is within this range of values and consistent with previously published winter to summer ratios of auroral parameters.

[40] To further substantiate our suggestion that the summer-time suppression of discrete aurora is more completely explained by the shorter timescales of substorms in sunlit conditions, we will examine the characteristics of the electron precipitation within each of the substorm phases

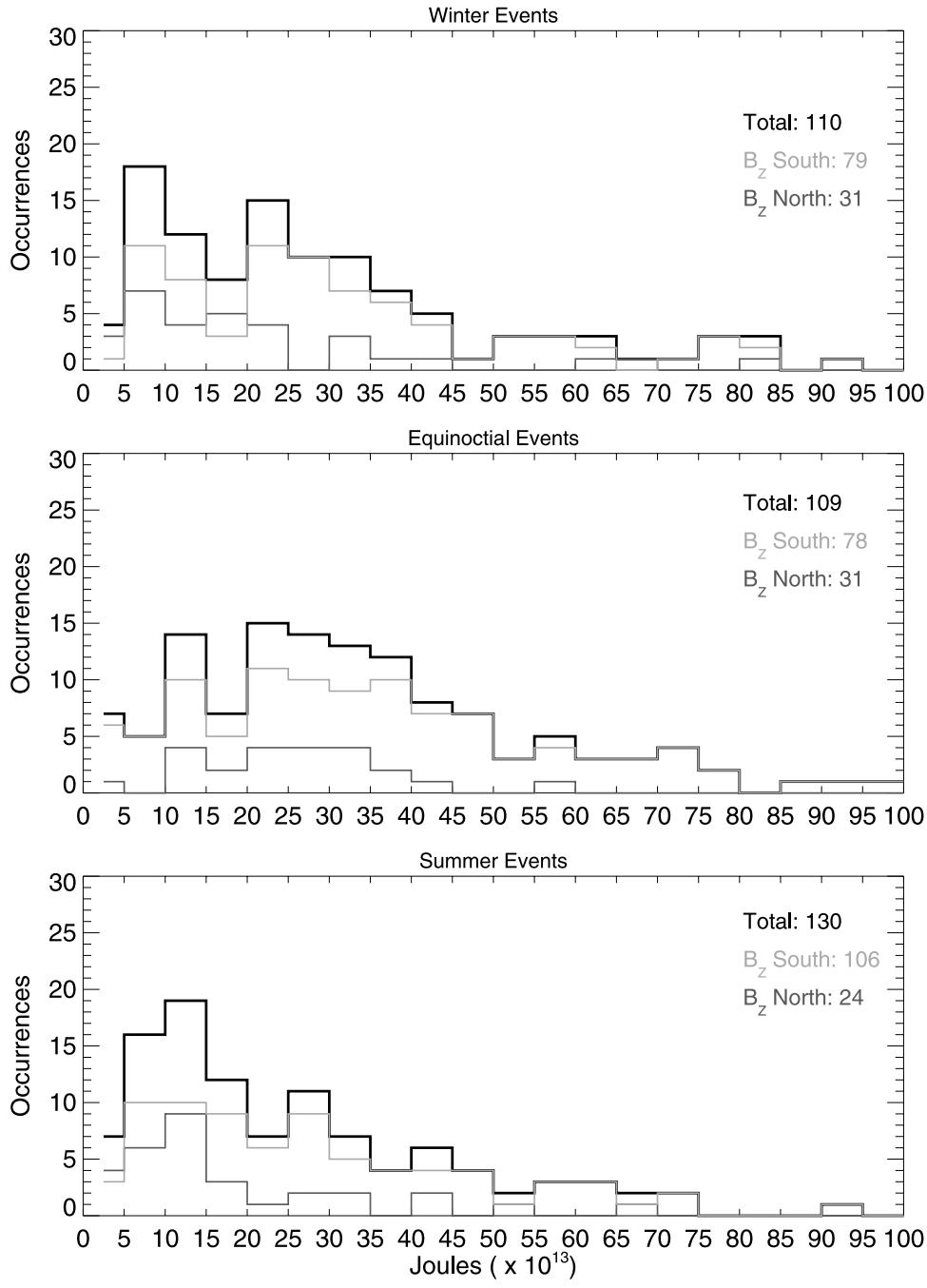

Figure 11. Histograms of total energy deposited by auroral electron precipitation, sorted by season.

Table 8. Statistics for Total Energy Deposition Sorted by Season

Total Energy Deposited	Mean, ($\times 10^{13}$Joules)	Median, ($\times 10^{13}$Joules)	Standard Deviation, ($\times 10^{13}$Joules)
Winter	31.0	23.9	24.6
Equinox	39.1	32.5	36.7
Summer	27.6	20.1	22.5

(epochs) defined here using the UVI derived hemispheric power in a forthcoming companion paper. Using coordinated Polar UVI and Fast Auroral Snapshot (FAST) [*Carlson et al.*, 1998] observations we will show in our next paper that discrete auroral forms are observed during summer-time substorms although over timescales shorter than those in winter-time or equinoctial events.

Appendix A: IMF Propagation and Orientation Determination

[41] The determination of the IMF orientation is made from Wind MFI [*Lepping et al.*, 1995] magnetic field measurements in GSM coordinates and Wind SWE [*Ogilvie et al.*, 1995] solar wind observations. These measurements are propagated in time from the Wind spacecraft location to an estimated subsolar, magnetopause location. For each event, the position of the subsolar magnetopause is calculated from a simple pressure balance method in which we assume that the dynamic pressure of the solar wind balances the magnetic pressure associated with the Earth's dipole:

$$nm_p u_x^2 = \frac{B^2}{2\mu_o} \tag{A1}$$

where B has the form

$$B = \frac{\mu_o M}{4\pi r^3}. \tag{A2}$$

In neglecting minor solar wind species, we take n to be the solar wind proton density, m_p is the proton mass, u_x is the x-component of the solar wind convection velocity, and M is the Earth's dipole moment. When substituting equation (A2) into equation (A1) and solving for r, the subsolar magnetopause location is given by

$$r_{mp} = \left(\frac{\mu_o M^2}{32\pi^2 nm_p u_x^2}\right)^{\frac{1}{6}} \tag{A3}$$

The IMF is propagated from the Wind spacecraft position to r_{mp} using the simple X-distance propagation method described by *Ridley* [2000]. Here the propagation time is simply given by the distance from the WIND spacecraft to r_{mp} divided by the x-component of the solar wind convection velocity. The uncertainty of this propagation time is computed using the result of *Ridley* [2000] who found that the maximum error of this propagation time is directly proportional to the off-axis distance of the spacecraft away from the Sun-Earth line, D_{yz}. This uncertainty is given by $\Delta t_{max} = 0.96 D_{yz}$. We then compute T_o, the time of origin in the solar wind corresponding to the substorm onset time minus the propagation time. The interval (in minutes) in which we examine the IMF orientation is set at $T_o \pm (\Delta t_{max} + 60)$. The 60 minute window around the origin time is derived from previous studies which have empirically determined that the lag times between the arrival of a solar wind structure and the magnetospheric response is on the order of 30 to 90 minutes [e.g., *Bargatze et al.*, 1985; *Zhou and Tsurutani*, 2001]. Sixty minutes was chosen as a representative timescale. A substorm is determined to occur during northward (southward) IMF if the average value of B_Z is positive (negative) during this interval.

[42] **Acknowledgments.** The research at the University of Washington is supported in part by NASA grant NAG5-3170. Work at the University of Alabama in Huntsville was supported by subcontracts SA3527 and SA3216 from the University of California at Berkeley. This work was performed in part while D. Chua held a National Research Council Research Associateship Award at the Naval Research Laboratory.

[43] The Editor thanks Kan Liou and Steven M. Petrinec for their assistance in evaluating this manuscript.

References

Aikio, A. T., V. A. Sergeev, M. A. Shukhtina, L. I. Vagina, V. Angelopoulos, and G. D. Reeves (1999), Characteristics of pseudobreakups and substorms observed in the ionosphere, at geosynchronous orbit and in the midtail, *J. Geophys. Res.*, *104*, 12,263.

Akasofu, S.-I. (1964), The development of the auroral substorm, *Planet. Space Sci.*, *12*, 273.

Bargatze, L. F., D. N. Baker, R. L. McPherron, and J. E. W. Hones (1985), Magnetospheric impulse response for many levels of geomagnetic activity, *J. Geophys. Res.*, *90*, 6387.

Berko, F. W., and R. A. Hoffman (1974), Dependence of field-aligned electron precipitation occurrence on season and altitude, *J. Geophys. Res.*, *79*, 3749.

Caan, M. N., R. L. McPherron, and C. T. Russell (1977), Characteristics of the association between the interplanetary magnetic field and substorms, *J. Geophys. Res.*, *82*, 4837.

Carlson, C. W., R. F. Pfaff, and J. G. Watzin (1998), The Fast Auroral Snapshot Mission, *Geophys. Res. Lett.*, *25*, 2013.

Chua, D. (2002), Ionospheric influence on the global characteristics of electron precipitation during auroral substorms, Ph.D. thesis, Univ. of Wash., Seattle.

Chua, D., G. Parks, M. Brittnacher, W. Peria, G. Germany, J. Spann, and C. Carlson (2001), Energy characteristics of auroral electron precipitation: A comparison of substorms and pressure pulse related auroral activity, *J. Geophys. Res.*, *106*, 5945.

Elvey, C. T. (1957), Problems of auroral morphology, *Proc. Natl. Acad. Sci. USA*, *43*, 63.

Fillingim, M. O. (2002), Kinetic processes in the plasma sheet observed during auroral activity, Ph.D. thesis, Univ. of Wash., Seattle.

Fillingim, M. O., G. K. Parks, L. J. Chen, M. McCarthy, J. F. Spann, and R. P. Lin (2001), Comparison of plasma sheet dynamics during pseudobreakups and expansive aurora, *Phys. Plasmas*, *8*, 1127.

Fillingim, M. O., Y.-K. Tung, G. K. Parks, S. B. Mende, H. U. Frey, and T. J. Immel (2003), Local time displacement of substorm expansion in conjugate hemispheres, *Eos Trans. AGU*, *84*(46), Fall Meet. Suppl., Abstract SM24B-0599.

Germany, G. A., M. R. Torr, D. G. Torr, and P. G. Richards (1994), Use of FUV auroral emissions as diagnostic indicators, *J. Geophys. Res.*, *99*, 383.

Germany, G. A., J. F. Spann, G. K. Parks, M. J. Brittnacher, R. Elsen, L. Chen, D. Lummerzheim, and M. H. Rees (1998), Auroral observations from the Polar Ultraviolet Imager (UVI), in *Encounter Between Global Observations and Models in the ISTP Era*, *Geophys. Monogr. Ser.*, vol. 104, edited by J. Horwitz, D. Gallagher, and W. Peterson, p. 143, AGU, Washington, D. C.

Lepping, R. P., et al. (1995), The WIND magnetic field investigation, *Space Sci. Rev.*, *71*, 207.

Liou, K., C.-I. Meng, A. T. Y. Lui, P. T. Newell, M. Brittnacher, G. D. Reeves, R. R. Anderson, and K. Yumoto (1999), On relative timings in substorm onsets, *J. Geophys. Res.*, *104*, 22,807.

Liou, K., P. T. Newell, and C.-I. Meng (2001), Seasonal effects on auroral particle acceleration and precipitation, *J. Geophys. Res.*, *106*, 5531.

Lummerzheim, D., M. Brittnacher, D. Evans, G. A. Germany, G. K. Parks, M. H. Rees, and J. F. Spann (1997), High time resolution study of the hemispheric power carried by energetic electrons into the ionosphere during the May 19/20, 1996 auroral activity, *Geophys. Res. Lett.*, *24*, 987.

Lyons, L. R., G. T. Blanchard, J. C. Samson, R. P. Lepping, T. Yamamoto, and T. Moretto (1997), Coordinated observations demonstrating external substorm triggering, *J. Geophys. Res.*, *102*, 27,039.

Lyons, L. R., E. Zesta, J. C. Samson, and G. D. Reeves (2000), Auroral disturbances during the January 10, 1997 magnetic storm, *Geophys. Res. Lett.*, *27*, 3237.

McIntosh, D. H. (1959), On the annual variation of magnetic disturbances, *Philos. Trans. R. Soc. London*, *251*, 525.

Meng, C.-I., and K. Liou (2002), Global auroral power as an index for geospace disturbances, *Geophys. Res. Lett.*, *29*(12), 1600, doi:10.1029/2001GL013902.

Nakamura, R., D. N. Baker, T. Yamamoto, R. D. Belian, E. A. B. III, J. R. Benbrook, and J. R. Theall (1994), Particle and field signatures during pseudobreakup and major expansion onset, *J. Geophys. Res.*, *99*, 207.

Newell, P. T., C.-I. Meng, and K. M. Lyons (1996), Suppression of discrete aurorae by sunlight, *Nature*, *381*, 766.

Newell, P. T., R. A. Greenwald, and J. M. Ruohoniemi (2001a), The role of the ionosphere in aurora and space weather, *Rev. Geophys.*, *39*, 137.

Newell, P. T., K. Liou, T. Sotirelis, and C.-I. Meng (2001b), Auroral precipitation power during substorms: A Polar UVI based superposed epoch analysis, *J. Geophys. Res.*, *106*, 28,885.

Ogilvie, K. W., et al. (1995), SWE, a comprehensive plasma instrument for the Wind spacecraft, *Space Sci. Rev.*, *71*, 55.

Ohtani, S., et al. (1993), A multisatellite study of a pseudo-substorm onset in the near-Earth magnetotail, *J. Geophys. Res.*, *98*, 19,355.

Papitashvili, V. O., C. R. Clauer, F. Christiansen, Y. Kamide, V. G. Petrov, O. Rasmussen, and J. F. Watermann (2002), Near-conjugate magnetic substorms at very high latitudes observed by Greenland and Antarctic ground magnetometers and Ørsted satellite, in *Proceedings of the Sixth International Conference on Substorms*, edited by R. M. Winglee, p. 110, Univ. of Wash., Seattle.

Parks, G. K., L. J. Chen, M. Fillingim, R. P. Lin, D. Larson, and M. McCarthy (2002), A new framework for studying the relationship of aurora and plasma sheet dynamics, *J. Atmos. Terr. Phys.*, *64*, 115.

Petrinec, S. M., W. L. Imhof, D. L. Chenette, J. Mobilia, and T. J. Rosenberg (2000), Dayside/nightside auroral X-ray emission differences - implications for ionospheric conductance, *Geophys. Res. Lett.*, *27*, 3277.

Pytte, T., R. L. McPherron, and S. Kokubun (1976), The ground signatures of the expansion phase during multiple onset substorms, *Planet. Space Sci.*, *24*, 1115.

Richmond, A. D. (1995), Ionospheric electrodynamics using magnetic apex coordinates, *J. Geomagn. Geoelectr.*, *47*, 191.

Ridley, A. J. (2000), Estimations of the uncertainty in timing the relationship between magnetospheric and solar wind processes, *J. Atmos. Sol. Terr. Phys.*, *62*, 757.

Rostoker, G. (1983), Triggering of expansive phase intensifications of magnetospheric substorms by northward turnings of the interplanetary magnetic field, *J. Geophys. Res.*, *88*, 6981.

Rostoker, G. (1996), Phenomonology and physics of magnetospheric substorms, *J. Geophys. Res.*, *101*, 12,955.

Rostoker, G., S.-I. Akasofu, W. Baumjohann, Y. Kamide, and R. L. McPherron (1987), The roles of direct input of energy from the solar wind and unloading of the stored magnetotail energy in driving magnetospheric substorms, *Space Sci. Rev.*, *46*, 93.

Saito, T. (1969), Geomagnetic pulsations, *Space Sci. Rev.*, *10*, 319.

Sergeev, V. A., A. G. Yahnin, R. A. Rakhmatulin, S. I. Solovjev, F. S. Mozer, D. J. Williams, and C. T. Russell (1986), Permanent flare activity in the auroral zone, *Planet. Space Sci.*, *34*, 1169.

Shue, J.-H., P. T. Newell, K. Liou, and C.-I. Meng (2001), The quantitative relationship between auroral brightness and solar EUV Pedersen conductance, *J. Geophys. Res.*, *106*, 5883.

Takahashi, K., S. Ohtani, and B. J. Anderson (1995), Statistical analysis of Pi2 pulsations observed by the AMPTE CCE spacecraft in the inner magnetosphere, *J. Geophys. Res.*, *100*, 21,929.

Taylor, J. R. (1982), *An Introduction to Error Analysis, The Study of Uncertainties in Physical Measurements*, Univ. Science Books, Herndon, Va.

Torr, M. R., et al. (1995), A far ultraviolet imager for the International Solar-Terrestrial Physics Mission, *Space Sci. Rev.*, *71*, 329.

Vorobjev, V. G., O. I. Yagodkina, D. Sibeck, K. Liou, and C.-I. Meng (2001), Aurora conjugacy during substorms: Coordinated Antarctic ground and Polar Ultraviolet observations, *J. Geophys. Res.*, *106*, 24,579.

Weimer, D. R. (1994), Substorm time constants, *J. Geophys. Res.*, *99*, 11,005.

Zandt, T. E. V., W. L. Clark, and J. M. Warnock (1972), Magnetic apex coordinates: A magnetic coordinate system for the ionospheric F2 layer, *J. Geophys. Res.*, *77*, 2406.

Zhou, X., and B. T. Tsurutani (2001), Interplanetary shock triggering of nightside geomagnetic activity: Substorms, pseudobreakups, and quiescent events, *J. Geophys. Res.*, *106*, 18,957.

M. Brittnacher, Department of Earth and Space Sciences, Box 351310, University of Washington, Seattle, WA 98195, USA.

D. Chua, Naval Research Laboratory, Code 7607, Washington, D. C., 20375, USA. (dchua@ssd5.nrl.navy.mil)

G. Germany, CSPAR, University of Alabama in Huntsville, Huntsville, AL 35899, USA.

G. Parks, Space Sciences Laboratory, University of California, Berkeley, CA 94720, USA.

J. Spann, NASA Marshall Space Flight Center, Huntsville, AL 35812, USA.